

# Resolving the eccentricity of stellar mass binary black holes with next generation gravitational wave detectors

Pankaj Saini <sup>\*</sup>

Chennai Mathematical Institute (CMI), Siruseri, 603103, India

Accepted XXX. Received YYY; in original form ZZZ

## ABSTRACT

Next generation gravitational wave (GW) detectors are expected to detect  $10^4$ – $10^5$  binary black holes (BBHs) per year. Understanding the formation pathways of these binaries is an open question. Orbital eccentricity can be used to distinguish between the formation channels of compact binaries as different formation channels are expected to yield distinct eccentricity distributions. Due to the rapid decay of eccentricity caused by the emission of GWs, measuring smaller values of eccentricity poses a challenge for current GW detectors due to their limited sensitivity. In this study, we explore the potential of next generation GW detectors such as Voyager, Cosmic Explorer (CE), and Einstein Telescope (ET) to resolve the eccentricity of BBH systems. Considering a GWTC-3 like population of BBHs and assuming some fiducial eccentricity distributions as well as an astrophysically motivated eccentricity distribution (Zevin *et al.* (2021)), we calculate the fraction of binaries that can be confidently distinguished as eccentric. We find that for Zevin eccentricity distribution, Voyager, CE, and ET can confidently measure the non-zero eccentricity for  $\sim 3\%$ ,  $9\%$ , and  $13\%$  of the detected BBHs, respectively. In addition to the fraction of resolvable eccentric binaries, our findings indicate that Voyager, CE, and ET require minimum eccentricities  $\gtrsim 0.02$ ,  $5 \times 10^{-3}$ , and  $10^{-3}$  at a GW frequency of 10 Hz, respectively, to identify a BBH system as eccentric. The better low-frequency sensitivity of ET significantly enhances its capacity to accurately measure eccentricity.

**Key words:** Gravitational waves – Binary black holes – Eccentricity

## 1 INTRODUCTION

The LIGO (Aasi *et al.* 2015) and Virgo (Acernese *et al.* 2015) have detected  $\mathcal{O}(100)$  compact binary mergers (Abbott *et al.* 2016, 2017c, 2019, 2020; Venumadhav *et al.* 2020; Abbott *et al.* 2021a,b; Nitz *et al.* 2021; Olsen *et al.* 2022; Nitz *et al.* 2023). One of the most interesting questions these observations are capable of answering is related to the formation scenarios of compact binaries, especially of binary black holes (BBHs) which will be observed in large numbers with the present and next generation GW detectors. There are broadly two formation channels of compact binaries: *isolated formation channel* and *dynamical formation channel* (Mapelli 2020, 2021; Mandel & Farmer 2022). In isolated formation channel, two massive stars in a binary system co-evolve in the galactic field, undergo supernova explosions and form BBHs. In the dynamical formation, a BBH is formed due to gravitational interaction in dense stellar environments such as globular and nuclear star clusters. The current observations of BBH mergers by LIGO and Virgo pose a challenge in terms of being explained solely through a single formation channel. A mixture of formation channels is preferred over a single formation channel (Abbott *et al.* 2021c; Bouffanais *et al.* 2021; Wong *et al.* 2021; Zevin *et al.* 2021a).

Future gravitational wave (GW) detectors with improved sensitivity will detect a large number of BBH mergers. For example, a LIGO

detector with Voyager technology is expected to detect  $\sim 10^4$  BBH mergers per year (Baibhav *et al.* 2019). Moreover, third-generation (3G) detectors such as Cosmic Explorer (CE) (Abbott *et al.* 2017a; Reitze *et al.* 2019) and Einstein Telescope (ET) (Punturo *et al.* 2010; Sathyaprakash *et al.* 2011; Maggiore *et al.* 2020) are expected to detect  $\sim 10^5$  BBH mergers per year (Baibhav *et al.* 2019; Evans *et al.* 2023; Gupta *et al.* 2023). Different formation channels leave unique imprints on the properties of BBH systems, providing valuable clues about their formation history.

Orbital eccentricity is one such unique feature that can give us clues about the formation channels of the binaries as different formation channels are expected to follow different eccentricity distributions. The ellipticity of a binary’s orbit at a given time depends on how these binaries formed. Since the emission of GWs carries away the energy and angular momentum from the binary system, with time, the elliptical orbits tend to become circular (Peters 1964). In the small eccentricity limit, the eccentricity approximately decreases with GW frequency as  $e_t/e_0 \approx (f_0/f)^{19/18}$  (Peters 1964). Here  $e_t$  is the “time-eccentricity” in the *quasi-Keplerian* representation of the binary orbit (Damour *et al.* 2004) when binary emits the GWs at dominant mode frequency  $f$ , and  $e_0$  is the initial value of  $e_t$  at a reference frequency  $f_0$ <sup>1</sup>. For example, a binary with an initial orbital eccentricity  $e_0 = 0.6$  when emitting GWs at 0.1 Hz reduces to one

<sup>1</sup> The definition of eccentricity is model dependent. One should ideally use a model-agnostic definition of eccentricity when comparing eccentricity mea-

<sup>\*</sup> E-mail: pankajsaini@cmi.ac.in

with eccentricity  $\sim 0.1$  when it enters the ET band at 1 Hz. The eccentricity reduces to  $\sim 0.02$  when it starts emitting GWs in the frequency band of CE and Voyager at 5 Hz. The eccentricity further reduces to  $\sim 5 \times 10^{-3}$  when it emits GWs at 20 Hz (the lower cut-off frequency of LIGO and Virgo).

In current GW detectors, the measurement of eccentricity for GW150914-like BBHs requires  $e_0 \gtrsim 0.05$  (at 10 Hz) (Lower et al. 2018; Favata et al. 2022). Next generation GW detectors with improved sensitivity will enable us to constrain smaller eccentricities. Apart from the overall improvement in sensitivity, 3G detectors will have excellent low-frequency sensitivity where binaries can retain a larger eccentricity. The potential of next generation GW detectors to measure orbital eccentricity remains unexplored. *In this paper, we study the ability of next generation GW detectors to constrain the eccentricity of binary black hole systems.*

Typically, binaries formed through isolated formation channels are expected to be in quasi-circular orbits by the time they enter the frequency band of ground-based detectors (Peters 1964; Hinder et al. 2008). Isolated binaries can have a non-negligible eccentricity due to the large natal kick imparted due to the second supernova. However, it happens well before the merger that the binary is likely to shed away all its eccentricity by the time it is observed in the frequency band of the ground-based detector. N-body simulations suggest that the formation of highly eccentric binaries is inevitable in dense stellar environments (Antonini & Perets 2012; Antonini et al. 2014, 2016; Rodriguez et al. 2018b). Dynamically formed binaries in dense star clusters such as globular star clusters, nuclear star clusters, and in the vicinity of supermassive black holes can retain moderate to high values of eccentricity when observed in the frequency band of ground-based detectors (Wen 2003; O’Leary et al. 2009; Bae et al. 2014; Samsing et al. 2014; Zevin et al. 2017; Samsing 2018; Gondán et al. 2018; Rodriguez et al. 2018b; Rasskazov & Kocsis 2019; Zevin et al. 2019; Gröbner et al. 2020; Tagawa et al. 2021; Zevin et al. 2021b; Dall’Amico et al. 2023). The gravitational interaction of a binary system with the third body can also increase its eccentricity (Sillsbee & Tremaine 2017; Liu & Lai 2018; Hoang et al. 2018). Around 5% of all dynamical mergers in globular clusters can give rise to BBHs with eccentricities  $\gtrsim 0.1$  at 10 Hz GW frequency<sup>2</sup> (Samsing & Ramirez-Ruiz 2017; Samsing & D’Orazio 2018; Samsing 2018; Rodriguez et al. 2018a; Rodriguez et al. 2018b).

There are already claims for the presence of eccentricity in the detected GW events (Romero-Shaw et al. 2020, 2021; O’Shea & Kumar 2021; Gayathri et al. 2022; Romero-Shaw et al. 2022). However, the eccentricity can be mimicked by spin-precession effects. Due to the lack of an inspiral-merger-ringdown waveform model that includes both eccentricity and spin-precession, it is hard to distinguish between the two effects, especially for the short signals such as GW190521 (Romero-Shaw et al. 2023).

Apart from the eccentricity, the spin orientation of the component BHs in a binary can also be used to discern between different formation channels (Rodriguez et al. 2016a; Stevenson et al. 2017; Talbot & Thrane 2017a; Vitale et al. 2017; Farr et al. 2017; O’Shaughnessy et al. 2017; Farr et al. 2018; Gerosa et al. 2018a; Gerosa et al. 2018b). Due to tidal interactions, isolated binaries are expected to have their spins aligned with the orbital angular momentum of the binary. However, dynamically formed BBHs are likely to have their spins

measurements from different analyses (Bonino et al. 2023; Arif Shaikh et al. 2023).

<sup>2</sup> The unmodeled binary eccentricity will potentially bias our parameter estimation [see for e.g. (Favata 2014; Favata et al. 2022; Saini et al. 2022; Bhat et al. 2023)].

misaligned. Hence these BBHs are expected to have isotropic spin distribution (Rodriguez et al. 2016b). Redshift evolution of merger rate can also be used to constrain formation scenarios (Rodriguez & Loeb 2018; Fishbach et al. 2018; Ng et al. 2022).

Here, we focus on the measurement of eccentricity. If the eccentricity of a BBH system is measured with relative error  $\Delta e_0/e_0 < 1$ , we will call it a *resolved binary*. This study examines the ability of Voyager, CE, and ET to measure the eccentricity of BBHs, drawn from a particular eccentricity distribution. More precisely, considering few fiducial eccentricity distributions as well as an astrophysically motivated eccentricity distribution given in Zevin et al. (2021b), we quantify the fraction of detected binaries that can be confidently identified as eccentric. In Section 2, we discuss the GW detectors considered in the study, the simulated binary black hole population, the details of the Fisher analysis, and the eccentric waveform model that we use for the analysis. Section 3 describes the results of the paper. Section 4 provides the summary and outlook of the study. Throughout the paper, we use units  $G = c = 1$ .

## 2 DETECTORS, BINARY BLACK HOLE POPULATION, AND METHODOLOGY

### 2.1 Detectors

We consider three ground-based GW detector configurations:

- (i) A LIGO detector operating at the Voyager sensitivity (Adhikari et al. 2020) with lower cut-off frequency  $f_{\text{low}} = 5$  Hz.
- (ii) Cosmic Explorer (CE) (Reitze et al. 2019) in USA with 40 km arm length at its design sensitivity. The lower cut-off frequency is chosen to be  $f_{\text{low}} = 5$  Hz.
- (iii) Einstein telescope (ET) (Punturo et al. 2010) in Europe with 10 km arm length at its design sensitivity. This will be an underground facility with a triangular shape. The lower cut-off frequency is taken to be  $f_{\text{low}} = 1$  Hz.

### 2.2 Binary black hole population

We consider a GWTC-3 like population of stellar mass binary black holes with the following distributions:

- *Primary mass*: The primary mass ( $m_1$ ) of binary black hole population follows PowerLaw+Peak model (Abbott et al. 2023) which is a mixture of a powerlaw and a Gaussian distribution (Talbot & Thrane 2017b). The values of parameters defining the PowerLaw+Peak model are taken to be:  $\lambda_{\text{peak}} = 0.04$ ,  $\alpha = 3.4$ ,  $m_{\text{min}} = 5.08$ ,  $m_{\text{max}} = 86.85$ ,  $\mu_m = 33.73$ ,  $\sigma_m = 3.56$ ,  $\delta_m = 4.83$ .
- *Mass ratio*: The mass ratio of BBH population follows a power law distribution  $p(q) = q^\beta$  with  $\beta = 1.08$ .
- *Spins*: We assume that the spin angular momentum vectors of binary components are aligned with the orbital angular momentum vector of the binary (non-precessing). The magnitudes of dimensionless spins for both black holes are drawn from a Beta distribution (Talbot & Thrane 2017b)

$$p(\chi_{1,2}|\alpha_\chi, \beta_\chi) \propto \chi_{1,2}^{\alpha_\chi-1} (1 - \chi_{1,2})^{\beta_\chi-1}, \quad (1)$$

where  $\alpha_\chi$  and  $\beta_\chi$  are the shape parameters that determine the mean and variance of the distribution. The values are  $\alpha_\chi = 1.6$ ,  $\beta_\chi = 4.11$ .

**Table 1.** Eccentricity distributions considered in this study. The initial eccentricity  $e_0$  is defined at 10 Hz GW frequency.

Eccentricity distribution	Loguniform	Powerlaw	Zevin
PDF	$p(e_0) \propto e_0^{-1}$	$p(e_0) \propto e_0^{-1.2}$	
Range of $e_0$	$(10^{-4} - 0.2)$	$(10^{-4} - 0.2)$	$(10^{-7} - 0.2)$
	$(10^{-7} - 0.2)$	$(10^{-7} - 0.2)$	

- *Eccentricity distributions:* Table 1 summarizes the eccentricity distributions considered in this study. We consider two fiducial eccentricity distributions: `Loguniform` and `Powerlaw` with two eccentricity ranges  $e_0 \in (10^{-4}, 0.2)$  and  $e_0 \in (10^{-7}, 0.2)$ . The upper limit of the distribution is fixed to be  $e_0 = 0.2$ , beyond which the waveform model employed in this study becomes less accurate. We also consider an expected astrophysical eccentricity distribution based on cluster simulations given in Fig. 1 of Zevin et al. (2021b). This will be referred to as `Zevin` eccentricity distribution from here onwards. The Fig. 1 of Zevin et al. (2021b) contains two eccentricity distributions plotted by dashed and solid lines. We use the eccentricity distribution shown in dashed lines which represents the intrinsic eccentricity distribution of the considered population. Similar to the `Loguniform` and `Powerlaw` eccentricity distributions, we restrict `Zevin` eccentricity distribution to the range  $e_0 \in (10^{-7}, 0.2)$ . Note that `Zevin` eccentricity distribution is based on cluster simulations which are based on many astrophysical assumptions. We draw eccentricity samples from the one-dimensional marginalized distribution and do not account for the correlations of eccentricity with other source parameters assuming them to be small.

- *Redshift:* Sources are distributed uniformly in comoving volume according to the following redshift distribution

$$p(z) \propto \frac{1}{1+z} \frac{dV_c}{dz}. \quad (2)$$

where  $\frac{dV_c}{dz}$  is the comoving volume element at redshift  $z$ . The factor  $(1+z)^{-1}$  converts the detector frame time to the source frame time. We choose maximum redshift  $z_{\max} = 2.5$  which corresponds to a luminosity distance  $d_L = 20.9$  Gpc. The corresponding  $d_L$  is calculated assuming Planck18 (Aghanim et al. 2020) cosmology using Astropy (Astropy Collaboration et al. 2018).

### 2.3 Methodology

Using the binary black hole population discussed in Sec. 2.2, we calculate measurement uncertainties on binary parameters. The statistical errors on binary parameters can be forecasted using the *Fisher information matrix* framework (Finn 1992; Cutler & Flanagan 1994; Poisson & Will 1995). This framework gives the  $1\sigma$  width around the injected values of the binary parameters. The inner product between two frequency domain signals  $\tilde{h}_1(f)$  and  $\tilde{h}_2(f)$  is defined as

$$(h_1|h_2) = 2 \int_{f_{\text{low}}}^{f_{\text{high}}} \frac{\tilde{h}_1^*(f)\tilde{h}_2(f) + \tilde{h}_1(f)\tilde{h}_2^*(f)}{S_n(f)} df, \quad (3)$$

where  $S_n(f)$  is the one-sided noise power spectral density (PSD) of the detector and  $*$  represents the complex conjugation. The limits of integration in Eq. (3) are fixed by the sensitivity of the detector and the properties of the source. The signal-to-noise ratio (SNR)  $\rho$

**Table 2.** Fraction of binaries that are detected with  $\text{SNR} \geq 8$ . The median value of five independent realisations is quoted. The median value is rounded to its nearest integer value.

Detector	Fraction of detected binaries (%)
<b>Voyager</b>	33
<b>CE</b>	100
<b>ET</b>	97

is defined as the norm of the signal,

$$\rho^2 = (h|h) = 4 \int_{f_{\text{low}}}^{f_{\text{high}}} \frac{|\tilde{h}(f)|^2}{S_n(f)} df, \quad (4)$$

The Fisher information matrix  $\Gamma_{ab}$  is defined as

$$\Gamma_{ab} = \left( \frac{\partial h}{\partial \theta_a} \middle| \frac{\partial h}{\partial \theta_b} \right). \quad (5)$$

where  $\theta_a$  is the set of waveform parameters. The covariance matrix is given as

$$\Sigma_{ab} = \Gamma_{ab}^{-1}, \quad (6)$$

$1\sigma$  errors on binary parameters  $\theta_a$  are calculated by taking the square root of the diagonal elements of the covariance matrix

$$\Delta\theta_a = \sqrt{\Sigma_{aa}}. \quad (7)$$

We use `TaylorF2Ecc` waveform model (Moore et al. 2016) which is an inspiral waveform model and accounts for the leading order  $[\mathcal{O}(e_0^2)]$  corrections due to eccentricity in the phasing expression. The `TaylorF2Ecc` waveform model is valid for small eccentricities  $e_0 \leq 0.2$ . The waveform model does not account for the eccentricity corrections to the amplitude. Since GW detectors are more sensitive to the GW phase than to the amplitude, small eccentricity corrections to the amplitude will be less important than eccentric corrections to the phase. The full expression for GW phasing can be found in Eq. (6.26) of (Moore et al. 2016). The circular part of Eq. (6.26) in (Moore et al. 2016) is for non-spinning binaries. We add aligned-spin terms to the circular part of Eq. (6.26) (Arun et al. 2005, 2009; Buonanno et al. 2009; Mishra et al. 2016).

The lower limit of integration ( $f_{\text{low}}$ ) in Eq. (3) is set by the lower cut-off frequency of the detector. For `Voyager`<sup>3</sup> and `CE`,  $f_{\text{low}}$  is set to be 5 Hz. For `ET`,  $f_{\text{low}}$  is taken to be 1 Hz. The upper cut-off frequency ( $f_{\text{high}}$ ) is the redshifted frequency corresponding to the innermost stable circular orbit ( $f_{\text{isco}}$ ) of the remnant Kerr BH (Bardeen et al. 1972; Husa et al. 2016; Hofmann et al. 2016). The  $f_{\text{isco}}$  is a function of two component masses and spins. The full expression can be found in Appendix C of (Favata et al. 2022). For `CE`, we use the noise PSD from (Abbott et al. 2017b). The analytical fit for `CE` noise PSD is given in Eq. (3.7) of Ref. (Kastha et al. 2018). For `ET`, we use design sensitivity `ET-D` (Hild et al. 2011). The `ET` noise PSD is scaled by a factor of  $(\sin^2 60^\circ)^{-1}$  to convert it to the effective sensitivity of `ET`'s triangular design.

<sup>3</sup> The noise curve for `Voyager` is taken to be `voyager.cb.txt` file from <https://dcc.cosmicexplorer.org/public/0163/T2000007/005/> inside `ce.curves.zip`.

Eccentricity distribution	Fraction (in %) of detected binaries with $\Delta e_0/e_0 < 1$		
	Voyager	CE	ET
<b>Loguniform(<math>10^{-4}, 0.2</math>)</b>	14	36	55
<b>Loguniform(<math>10^{-7}, 0.2</math>)</b>	8	20	30
<b>Powerlaw(<math>10^{-4}, 0.2</math>)</b>	7	20	37
<b>Powerlaw(<math>10^{-7}, 0.2</math>)</b>	2	5	9
<b>Zevin(<math>10^{-7}, 0.2</math>)</b>	3	9	13

**Table 3.** The fraction of detected binaries that are measured with  $\Delta e_0/e_0 < 1$ . To account for statistical fluctuations of the results, the exercise is carried out five times and the median values are reported.

### 3 RESULTS

In this section, we examine the capability of Voyager, CE, and ET to measure orbital eccentricity. First, we calculate the fraction of total sources that are detected in each detector above a certain threshold SNR. In Sec. 3.1, we quantify the fraction of detected sources that can be resolved. To recall, a binary with  $\Delta e_0/e_0 < 1$  is called *resolved binary*. We show the cumulative distribution of resolved binaries for each eccentricity distribution in Sec. 3.2. In Sec. 3.3, we investigate the minimum values of eccentricity that can be measured with Voyager, CE, and ET.

#### 3.1 Fraction of detected binaries with resolved eccentricity

We draw 20000 binary black hole samples from mass, spin, eccentricity, and redshift distributions discussed in Sec. 2.2. For Voyager, CE, and ET, we calculate the SNR for all these sources. The detection threshold is set to be  $\rho_{\text{th}} \geq 8$  for all the detectors. The fraction of sources that are detected in Voyager, CE, and ET with  $\rho_{\text{th}} \geq 8$  are summarized in Table 2. For each detector, we perform five independent realisations of the simulation and quote the median value of the fraction of detected binaries. Voyager detects 33% of the total sources, while CE and ET detect 100% and 97% of the total sources with  $\rho_{\text{th}} \geq 8$ , respectively. The sources that do not pass the detection threshold are discarded from further analysis.

For detected binaries, we calculate  $1\sigma$  errors on binary parameters using the Fisher information matrix. Table 3 shows the fraction of detected binaries for which eccentricity can be resolved. A source with  $\Delta e_0/e_0 < 1$  can be called eccentric with  $\geq 68\%$  confidence. The value quoted is the median value of the five independent realisations. Among all eccentricity distributions, Loguniform( $10^{-4}, 0.2$ ) represents the maximum number of resolved sources for all three detectors. This is because Loguniform( $10^{-4}, 0.2$ ) has the maximum number of sources with higher eccentricity. For this eccentricity distribution, Voyager can confidently measure non-zero eccentricity for 14% of the detected sources. CE can resolve 36% of the sources, while ET can resolve eccentricity for 55% of the sources. The number of resolved binaries in ET is  $\sim 1.5$  times larger than CE and  $\sim 4$  times larger than Voyager. This is due to the longer inspiral of the GW signal and better low-frequency sensitivity of ET. The effect of the lower cut-off frequency of ET on the fraction of resolved binaries is shown in Appendix A.

For Loguniform( $10^{-7}, 0.2$ ), Voyager can resolve 8% of the detected sources, while CE and ET resolve 20% and 30% of the detected sources, respectively. Lowering the lower limit of eccentricity distribution to  $e_0 = 10^{-7}$  reduces the number of sources with higher eccentricity. Therefore, the number of resolved binaries reduces by a factor of  $\sim 2$  compared to Loguniform( $10^{-4}, 0.2$ ). ET

can still resolve the eccentricity for 30% of the detected sources for Loguniform( $10^{-7}, 0.2$ ).

For Powerlaw( $10^{-4}, 0.2$ ), the number of sources for which the eccentricity can be resolved becomes smaller by a factor of  $1.5 - 2$  compared to the Loguniform( $10^{-4}, 0.2$ ) distribution. ET can resolve 37% of the detected sources for Powerlaw( $10^{-4}, 0.2$ ). For Powerlaw( $10^{-7}, 0.2$ ), the number of resolved sources becomes  $\sim 4$  times smaller than the number for Powerlaw( $10^{-4}, 0.2$ ) for all detectors. ET will be able to resolve eccentricity for  $\sim 9\%$  of the sources for Powerlaw( $10^{-7}, 0.2$ ) distribution.

For Zevin( $10^{-7}, 0.2$ ) eccentricity distribution, Voyager can confidently distinguish 3% of the detected sources from circular binaries. CE can distinguish 9% of the sources as eccentric, while ET can resolve 13% of the detected sources. In Sec. 3.3, we investigate which part of the eccentricity distributions dominates the resolved binaries.

Eccentricity distributions based on N-body simulations (including Zevin eccentricity distribution) predict that a reasonable fraction of binaries can retain  $e_0 > 0.2$  at 10 Hz GW frequency. A binary with a higher value of eccentricity is easier to be distinguished as eccentric. We do not include sources with  $e_0 > 0.2$  (at 10 Hz) in our analysis. Hence the fraction of resolved binaries quoted in table 3 represents a conservative lower limit.

#### 3.2 Fraction of resolved binaries with excellent eccentricity measurement

Having discussed the ability of GW detectors to constrain the fraction of different eccentricity distributions by resolving the eccentricity of binaries in Sec. 3.1, in this section, we discuss the cumulative distribution of  $\Delta e_0/e_0$  for resolved binaries to get insight into the number of resolved binaries and their corresponding measurement precision. Figure 1 shows the cumulative probability distributions of  $\Delta e_0/e_0$  for resolved binaries. Different panels show different eccentricity distributions. Three curves in different colours represent three GW detectors: Voyager, CE, and ET. Each curve consists of five thin curves which represent five independent realisations.

For all eccentricity distributions, ET measures eccentricity for the larger number of sources with smaller errors followed by CE and Voyager. For Loguniform( $10^{-4}, 0.2$ ) distribution, Voyager is able to measure  $\sim 20\%$  of the resolved binaries with precision better than 10%. While CE and ET can measure  $\sim 60\%$  and  $\sim 75\%$  of the resolved sources with a precision better than 10%, respectively. For Loguniform( $10^{-7}, 0.2$ ), the fraction of resolved sources is similar to Loguniform( $10^{-4}, 0.2$ ) distribution. It is important to stress that though the fraction of resolved binaries is similar for Loguniform( $10^{-4}, 0.2$ ) and Loguniform( $10^{-7}, 0.2$ ), the number of resolved binaries is less for Loguniform( $10^{-7}, 0.2$ ) compared to Loguniform( $10^{-4}, 0.2$ ). For Powerlaw( $10^{-4}, 0.2$ ), the fractions of

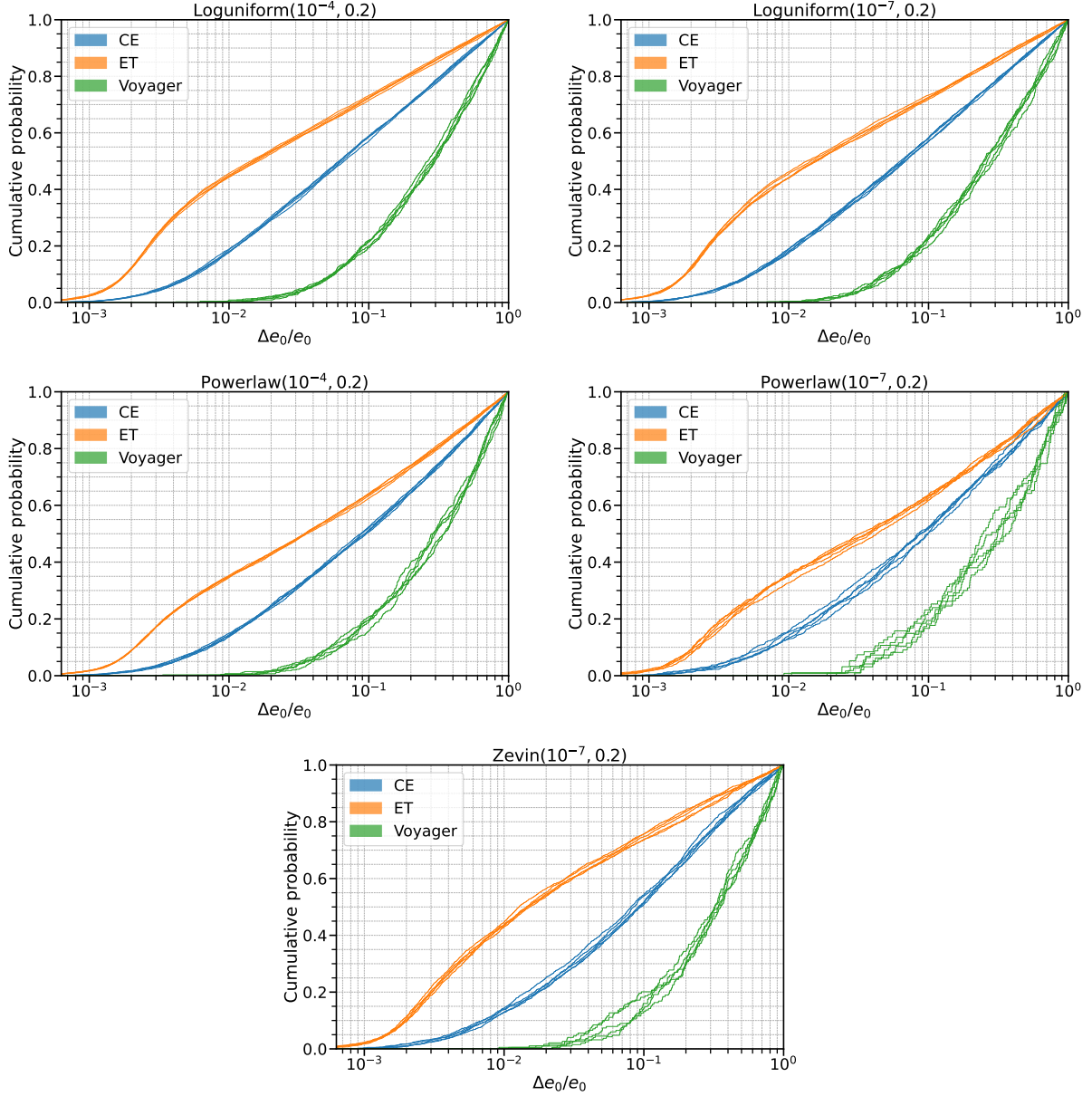


**Figure 1.** The cumulative probability distribution of  $\Delta e_0/e_0$  for resolved binaries. Different panels show different eccentricity distributions. Three colours in each panel represent different GW detectors. For each detector, thin lines with the same colour represent five different realisations of the population. Einstein Telescope measures a larger fraction of binaries with smaller errors for all eccentricity distributions. The lower frequency cut-off frequency ( $f_{\text{low}}$ ) for Voyager and CE is 5 Hz. For ET,  $f_{\text{low}} = 1$  Hz.

resolved sources with precision better than 10% for Voyager, CE, and ET are  $\sim 20\%$ ,  $50\%$ , and  $65\%$ , respectively. The fractions of resolved binaries are similar for Loguniform( $10^{-7}$ , 0.2).

For the Zevin( $10^{-7}$ , 0.2) distribution, Voyager can measure the eccentricity of  $\sim 15\%$  of the resolved sources with accuracy better than 10%. CE measures  $\sim 52\%$  of the resolved sources with  $\Delta e_0/e_0 < 0.1$ , whereas ET measures eccentricity for  $\sim 75\%$  of the resolved sources (13%) with better than 10% precision. ET shows remarkable capabilities for measuring the eccentricity of binary black holes. The dependence of eccentricity measurement on the binary's eccentricity is explained in the next Section.

### 3.3 Minimum resolvable eccentricity for Voyager, Cosmic Explorer, and Einstein Telescope

To gain insights into the measured values of eccentricities and their corresponding precision, we plot  $e_0$  and  $\Delta e_0/e_0$  for resolved binaries in Fig. 2 for one of the (randomly chosen) realisations. Figure 2 shows the dependence of eccentricity measurement on binary's eccentricity. Five panels represent different eccentricity distributions. In each panel, distinct colours represent different detectors. For all eccentricity distributions, each detector takes a different region in  $(e_0, \Delta e_0/e_0)$  plane with ET measuring more number of sources with better precision followed by CE and Voyager. As expected, the most

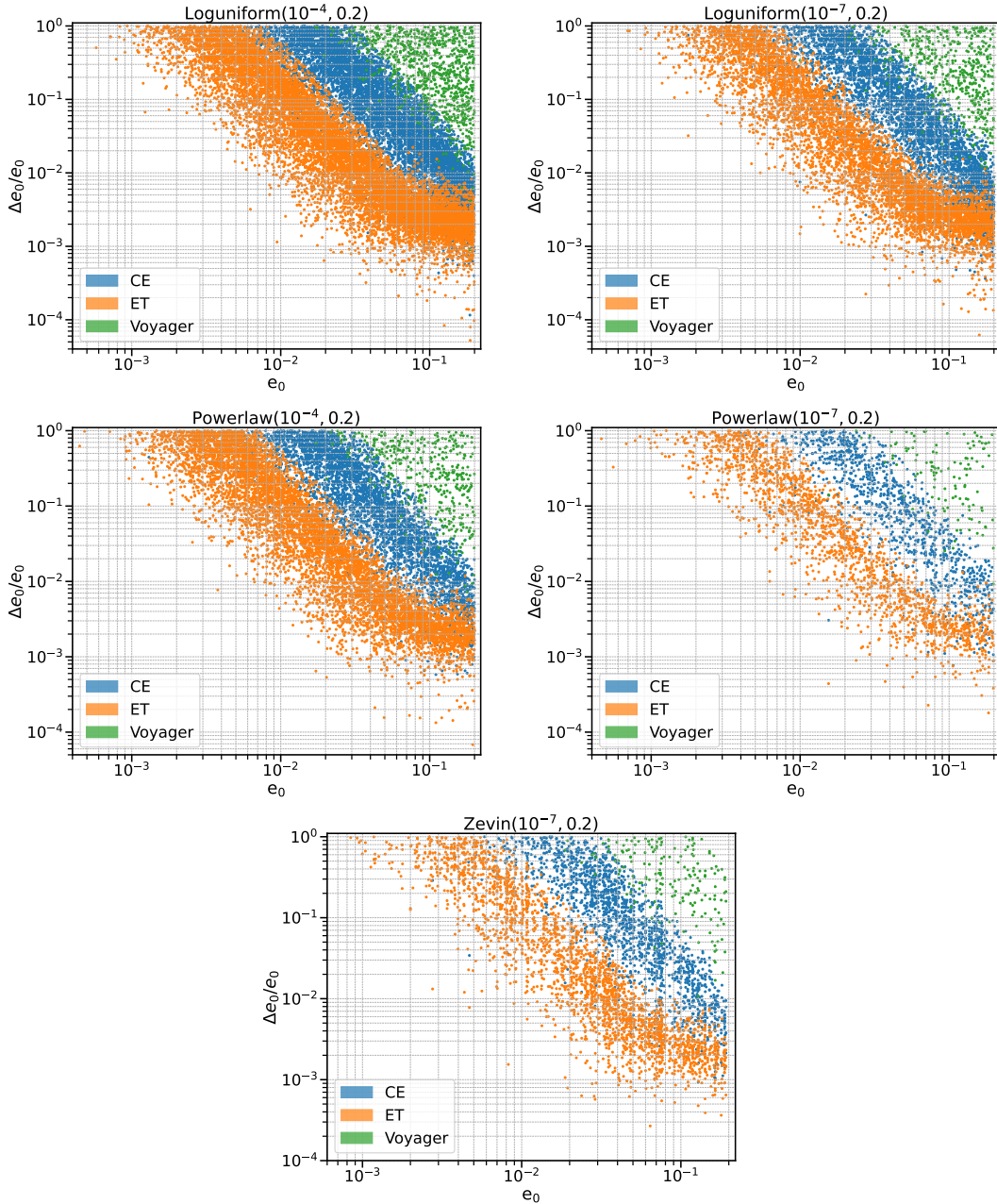


**Figure 2.** Scatter plots of  $\Delta e_0/e_0$  with  $e_0$  for those sources that have  $\Delta e_0/e_0 < 1$ . Each panel shows different eccentricity distributions. The distinct colours represent different detectors. The initial orbital eccentricity  $e_0$  on the x-axis is defined at a reference gravitational-wave (dominant mode) frequency of 10 Hz.

precise measurement of eccentricity comes from the larger eccentricities.

From the plots, it is clear that as the eccentricity increases, the  $\Delta e_0/e_0$  decreases. For ET, the fractional errors reduce to  $\sim 10^{-3} - 10^{-2}$  for high values of eccentricities ( $e_0 > 0.1$ ). For CE, a source with  $e_0 > 0.1$  can be measured with  $\Delta e_0/e_0 \sim 5 \times 10^{-3} - 0.1$ . Voyager can measure eccentricity greater than 0.1 with  $\Delta e_0/e_0 \sim 0.1 - 1$ . Notice that the number of sources with measured eccentricity is smaller for eccentricity distributions with a wider range ( $10^{-7}, 0.2$ ), as expected.

It can be observed from the figure that it requires  $e_0 \gtrsim 10^{-3}$  at 10 Hz GW frequency for ET to confidently distinguish a binary system

as eccentric. For CE and Voyager, it requires  $e_0 \gtrsim 5 \times 10^{-3}$  and  $e_0 \gtrsim 0.02$  (at 10 Hz GW frequency), respectively, to confidently measure a non-zero eccentricity. The better measurement of eccentricity by ET compared to CE is mainly due to two effects. The first is due to the better sensitivity of ET at low frequencies (below 8 Hz) compared to CE and the second is because the binary system has a relatively larger value of eccentricity when it enters the frequency band of ET (1 Hz). For example, a binary with  $e_0 = 0.05$  at 10 Hz GW frequency had an eccentricity of  $\sim 0.1$  when it entered the CE and Voyager band at 5

Hz. The binary had an eccentricity of 0.4 when entering the ET band at 1 Hz <sup>4</sup>. Hence ET provides better measurements of eccentricity.

It is clear that Voyager, CE, and ET can resolve only the *high eccentricity* part of the eccentricity distributions. None of the detectors is able to resolve eccentricity  $\lesssim 10^{-3}$  at 10 Hz GW frequency. In Zevin eccentricity distribution, the BBHs formed via GW capture have  $e_0 \gtrsim 10^{-3}$  at 10 Hz GW frequency. Hence next generation GW detectors such as Voyager, CE, and ET will be able to confidently distinguish a BBH system as eccentric that is likely formed via GW capture in globular clusters. However, there are other channels that can produce BBHs with  $e_0 \gtrsim 10^{-3}$  at 10 Hz. These include field triples undergoing Lidov-Kozai oscillations, three-body mergers in globular clusters, direct capture within galactic nuclei, and binaries formed near supermassive BHs (Antonini & Perets 2012; Antonini et al. 2017; Hoang et al. 2018; Lower et al. 2018). Though next generation GW detectors would be able to identify a BBH system as eccentric formed through these channels, distinguishing these formation scenarios from each other may be more challenging.

## 4 SUMMARY AND OUTLOOK

In this work, we have studied the ability of next generation GW detectors such as Voyager, CE, and ET to measure the eccentricity of binary black holes. The key goal was to investigate the fraction of detected binaries that can be confidently distinguished as eccentric by measuring a non-zero value of eccentricity. The precise measurement of eccentricity can be used to distinguish different formation channels as the eccentricity of a binary system depends on its formation history.

We find that for Zevin eccentricity distribution, Voyager can resolve the eccentricity for  $\sim 3\%$  of the detected BBHs. CE can resolve eccentricities for  $\sim 9\%$  of the detected BBHs, whereas ET can resolve the eccentricity of  $\sim 13\%$  of the detected BBHs. Moreover, a subpopulation of resolvable eccentric binary systems will have an extremely precise measurement of eccentricity. For Voyager, (15–20)% of the resolved binaries will have eccentricity measurement better than 10%, while for CE and ET, (50–60)% and (65–75)% of the resolved binaries will have  $\Delta e_0/e_0 \lesssim 10\%$ , respectively. ET’s low-frequency sensitivity plays a crucial role in the measurement of eccentricity.

Another important aspect of this study is the determination of the minimum value of eccentricity that is required to confidently identify a binary system as eccentric. We find that it requires eccentricities  $\gtrsim 0.02$  (at 10 Hz GW frequency) for Voyager to identify a binary as eccentric. For CE and ET, the minimum eccentricities that can be measured to distinguish a binary as eccentric are  $\gtrsim 5 \times 10^{-3}$  and  $\gtrsim 10^{-3}$  at 10 Hz GW frequency, respectively. In summary, next generation GW detectors would be able to confidently distinguish BBH systems with  $e_0 \gtrsim 10^{-3}$  (at 10 Hz GW frequency) from circular binaries.

Dynamically formed binaries are expected to have isotropic spin distribution. Our waveform model does not account for the precessional effect. Moreover, TaylorF2Ecc waveform model does not take into account the higher modes due to eccentricity. It would be interesting to study the effect of precession and higher modes (due to

eccentricity) on eccentricity measurement. The ability of GW detectors to reconstruct the actual eccentricity distribution can be explored in a future study.

## ACKNOWLEDGEMENTS

The author is grateful to K. G. Arun for valuable discussions and comments on the draft. We thank Michael Zevin for providing data to reproduce the eccentricity distribution of Zevin et al. (2021b). It is a pleasure to thank Anuradha Gupta, Sajad A. Bhat, Parthapratim Mahapatra, Poulami Dutta Roy, Nathan Johnson-McDaniel, and B. S. Sathyaprakash for useful discussions and/or comments on the draft. P. S. acknowledges partial support from the Infosys Foundation. Computations were performed on the CIT cluster provided by the LIGO Laboratory. This study made use of the following software packages: Astropy (Astropy Collaboration et al. 2013, 2018), Scipy (Virtanen et al. 2020), NumPy (Harris et al. 2020), Matplotlib (Hunter 2007), Seaborn (Waskom 2021), jupyter (Kluyver et al. 2016), pandas (Wes McKinney 2010).

## DATA AVAILABILITY

The data supporting the findings of this article will be made available upon reasonable request to the corresponding author.

## APPENDIX A: THE EFFECT OF EINSTEIN TELESCOPE LOWER CUT-OFF FREQUENCY ON THE FRACTION OF RESOLVED BINARIES

Due to the seismic noise, it might be hard to achieve sensitivity as low as 1 Hz for ET. Here, we study the impact of lower frequency cut-off on the eccentricity measurement. Table A1 shows the fraction of detected binaries with resolvable eccentricity ( $\Delta e_0/e_0 < 1$ ) for three frequency cut-offs:  $f_{\text{low}} = 1$  Hz,  $f_{\text{low}} = 3$  Hz, and  $f_{\text{low}} = 5$  Hz. The change of lower frequency cut-off has a significant effect on the resolved fraction of eccentric binaries.

For Loguniform( $10^{-4}, 0.2$ ), increasing the  $f_{\text{low}}$  from 1 Hz to 3 Hz, reduces the fraction of resolved binaries from 55% to 48% (a  $\sim 12\%$  change). Further, increasing  $f_{\text{low}}$  to 5 Hz, reduces the fraction to 40% ( $\sim 27\%$  change). Notice that for Loguniform( $10^{-4}, 0.2$ ), CE ( $f_{\text{low}} = 5$  Hz) can measure eccentricity for 35% of the detected sources. ET at  $f_{\text{low}} = 5$  Hz can resolve a larger fraction of eccentricity distribution compared to CE. This is because of the better low-frequency sensitivity of ET (below 8 Hz) compared to CE.

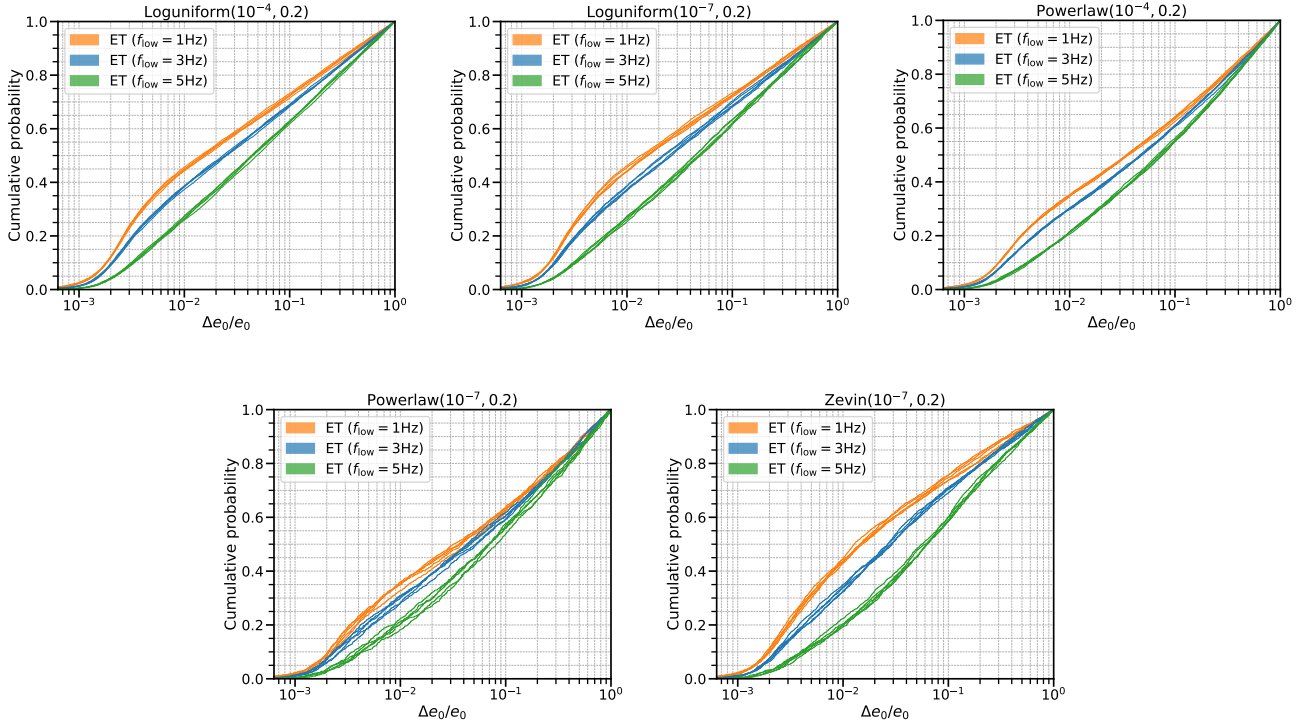
For Loguniform( $10^{-7}, 0.2$ ), there is a  $\sim 10\%$  and  $\sim 26\%$  reduction in the fraction of resolved sources when  $f_{\text{low}}$  is increased from 1 Hz to 3 Hz and 5 Hz, respectively. Similar kind of trends can be seen for Powerlaw( $10^{-4}, 0.2$ ) and Powerlaw( $10^{-7}, 0.2$ ) distributions. For Zevin eccentricity distribution, there is a 7% and 23% reduction in the fraction of resolved sources, when  $f_{\text{low}}$  is increased from 1 Hz to 3 Hz and 5 Hz, respectively.

Figure A1 shows the effect of  $f_{\text{low}}$  on the cumulative probability distribution of  $\Delta e_0/e_0 < 1$ . It can be seen that the number of sources with smaller errors reduces as the  $f_{\text{low}}$  increases from 1 Hz to 3 Hz and 5 Hz. Hence, the lower cut-off frequency of ET plays a critical role in the measurement of low-frequency effects such as eccentricity.

<sup>4</sup> It is worth noting that for few sources the value of  $e_0$  can become greater than 0.2 in the frequency band of the detector (especially for ET). The waveform model becomes less accurate for  $e_0 > 0.2$ . However, the number of sources with such high eccentricity is very small compared to the total number of sources.

Fraction (in %) of detected binaries with $\Delta e_0/e_0 < 1$			
Eccentricity distribution	ET ( $f_{\text{low}} = 1\text{Hz}$ )	ET ( $f_{\text{low}} = 3\text{Hz}$ )	ET ( $f_{\text{low}} = 5\text{Hz}$ )
<b>Loguniform (<math>10^{-4}, 0.2</math>)</b>	55	48	40
<b>Loguniform (<math>10^{-7}, 0.2</math>)</b>	30	27	22
<b>Powerlaw (<math>10^{-4}, 0.2</math>)</b>	37	30	23
<b>Powerlaw (<math>10^{-7}, 0.2</math>)</b>	9	7	6
<b>Zevin (<math>10^{-7}, 0.2</math>)</b>	13	12	10

**Table A1.** The effect of ET's lower cut-off frequency ( $f_{\text{low}}$ ) on the fraction of resolved binaries. The simulation is repeated five independent times and the median value is quoted. The  $f_{\text{low}}$  plays a crucial role in the eccentricity measurement.



**Figure A1.** The effect of ET's lower cut-off frequency on the cumulative probability distribution. The number of sources with smaller errors reduces as the  $f_{\text{low}}$  increases from 1 Hz to 3 Hz and 5 Hz.

## REFERENCES

- Aasi J., et al., 2015, *Class. Quant. Grav.*, 32, 074001
- Abbott B. P., et al., 2016, *Phys. Rev. Lett.*, 116, 061102
- Abbott B. P., et al., 2017a, *Class. Quant. Grav.*, 34, 044001
- Abbott B. P., et al., 2017b, *Classical and Quantum Gravity*, 34, 044001
- Abbott B. P., et al., 2017c, *Phys. Rev. Lett.*, 119, 161101
- Abbott B. P., et al., 2019, *Phys. Rev. X*, 9, 031040
- Abbott B. P., et al., 2020, *Astrophys. J. Lett.*, 892, L3
- Abbott R., et al., 2021a, arXiv preprint arXiv:2111.03606
- Abbott R., et al., 2021b, *Phys. Rev. X*, 11, 021053
- Abbott R., et al., 2021c, *Astrophys. J. Lett.*, 913, L7
- Abbott R., et al., 2023, *Phys. Rev. X*, 13, 011048
- Acernese F., et al., 2015, *Class. Quant. Grav.*, 32, 024001
- Adhikari R. X., et al., 2020, *Class. Quant. Grav.*, 37, 165003
- Aghanim N., et al., 2020, *Astron. Astrophys.*, 641, A6
- Antonini F., Perets H. B., 2012, *Astrophys. J.*, 757, 27
- Antonini F., Murray N., Mikkola S., 2014, *Astrophys. J.*, 781, 45
- Antonini F., Chatterjee S., Rodriguez C. L., Morscher M., Pattabiraman B., Kalogera V., Rasio F. A., 2016, *Astrophys. J.*, 816, 65
- Antonini F., Toonen S., Hamers A. S., 2017, *Astrophys. J.*, 841, 77
- Arif Shaikh M., Varma V., Pfeiffer H. P., Ramos-Buades A., van de Meent M., 2023, *arXiv e-prints*, p. arXiv:2302.11257
- Arun K. G., Iyer B. R., Sathyaprakash B. S., Sundararajan P. A., 2005, *Phys. Rev. D*, 71, 084008
- Arun K. G., Buonanno A., Faye G., Ochsner E., 2009, *Phys. Rev. D*, 79, 104023
- Astropy Collaboration et al., 2013, *A&A*, 558, A33
- Astropy Collaboration et al., 2018, *AJ*, 156, 123
- Bae Y.-B., Kim C., Lee H. M., 2014, *Mon. Not. Roy. Astron. Soc.*, 440, 2714
- Baibhav V., Berti E., Gerosa D., Mapelli M., Giacobbo N., Bouffanais Y., Di Carlo U. N., 2019, *Phys. Rev. D*, 100, 064060
- Bardeen J. M., Press W. H., Teukolsky S. A., 1972, *ApJ*, 178, 347
- Bhat S. A., Saini P., Favata M., Arun K. G., 2023, *Phys. Rev. D*, 107, 024009
- Bonino A., Gamba R., Schmidt P., Nagar A., Pratten G., Breschi M., Rettengo P., Bernuzzi S., 2023, *Phys. Rev. D*, 107, 064024
- Bouffanais Y., Mapelli M., Santoliquido F., Giacobbo N., Di Carlo U. N., Rastello S., Artale M. C., Iorio G., 2021, *Mon. Not. Roy. Astron. Soc.*, 507, 5224
- Buonanno A., Iyer B., Ochsner E., Pan Y., Sathyaprakash B. S., 2009, *Phys.*

- Rev. D, 80, 084043
- Cutler C., Flanagan E. E., 1994, *Phys. Rev. D*, 49, 2658
- Dall’Amico M., Mapelli M., Torniamenti S., Arca Sedda M., 2023, *arXiv e-prints*, p. [arXiv:2303.07421](https://arxiv.org/abs/2303.07421)
- Damour T., Gopakumar A., Iyer B. R., 2004, *Phys. Rev. D*, 70, 064028
- Evans M., et al., 2023, *arXiv preprint arXiv:2306.13745*
- Farr W. M., Stevenson S., Coleman Miller M., Mandel I., Farr B., Vecchio A., 2017, *Nature*, 548, 426
- Farr B., Holz D. E., Farr W. M., 2018, *Astrophys. J. Lett.*, 854, L9
- Favata M., 2014, *Phys. Rev. Lett.*, 112, 101101
- Favata M., Kim C., Arun K. G., Kim J., Lee H. W., 2022, *Phys. Rev. D*, 105, 023003
- Finn L. S., 1992, *Phys. Rev. D*, 46, 5236
- Fishbach M., Holz D. E., Farr W. M., 2018, *ApJ*, 863, L41
- Gayathri V., et al., 2022, *Nature Astron.*, 6, 344
- Gerosa D., Berti E., O’Shaughnessy R., Belczynski K., Kesden M., Wysocki D., Gladysz W., 2018a, *Phys. Rev. D*, 98, 084036
- Gerosa D., Berti E., O’Shaughnessy R., Belczynski K., Kesden M., Wysocki D., Gladysz W., 2018b, *Phys. Rev. D*, 98, 084036
- Gondán L., Kocsis B., Raffai P., Frei Z., 2018, *Astrophys. J.*, 860, 5
- Gröbner M., Ishibashi W., Tiwari S., Haney M., Jetzer P., 2020, *Astron. Astrophys.*, 638, A119
- Gupta I., et al., 2023, *arXiv preprint arXiv:2307.10421*
- Harris C. R., et al., 2020, *Nature*, 585, 357
- Hild S., et al., 2011, *Class. Quant. Grav.*, 28, 094013
- Hinder I., Vaishnav B., Herrmann F., Shoemaker D. M., Laguna P., 2008, *Phys. Rev. D*, 77, 081502
- Hoang B.-M., Naoz S., Kocsis B., Rasio F. A., Dosopoulou F., 2018, *ApJ*, 856, 140
- Hofmann F., Barausse E., Rezzolla L., 2016, *Astrophys. J. Lett.*, 825, L19
- Hunter J. D., 2007, *Computing in Science & Engineering*, 9, 90
- Husa S., Khan S., Hannam M., Pürrer M., Ohme F., Jiménez Forteza X., Bohé A., 2016, *Phys. Rev. D*, 93, 044006
- Kastha S., Gupta A., Arun K. G., Sathyaprakash B. S., Van Den Broeck C., 2018, *Phys. Rev. D*, 98, 124033
- Kluyver T., et al., 2016, in Loizides F., Schmidt B., eds, *Positioning and Power in Academic Publishing: Players, Agents and Agendas*. IOS Press, pp 87–90, <https://eprints.soton.ac.uk/403913/>
- Liu B., Lai D., 2018, *Astrophys. J.*, 863, 68
- Lower M. E., Thrane E., Lasky P. D., Smith R., 2018, *Phys. Rev. D*, 98, 083028
- Maggiore M., et al., 2020, *JCAP*, 03, 050
- Mandel I., Farmer A., 2022, *Phys. Rept.*, 955, 1
- Mapelli M., 2020, *Proc. Int. Sch. Phys. Fermi*, 200, 87
- Mapelli M., 2021, *Formation Channels of Single and Binary Stellar-Mass Black Holes*. ([arXiv:2106.00699](https://arxiv.org/abs/2106.00699)), [doi:10.1007/978-981-15-4702-7\\_16-1](https://doi.org/10.1007/978-981-15-4702-7_16-1)
- Mishra C. K., Kela A., Arun K. G., Faye G., 2016, *Phys. Rev. D*, 93, 084054
- Moore B., Favata M., Arun K. G., Mishra C. K., 2016, *Phys. Rev. D*, 93, 124061
- Ng K. K. Y., et al., 2022, *Astrophys. J. Lett.*, 931, L12
- Nitz A. H., Capano C. D., Kumar S., Wang Y.-F., Kastha S., Schäfer M., Dhurkunde R., Cabero M., 2021, *ApJ*, 922, 76
- Nitz A. H., Kumar S., Wang Y.-F., Kastha S., Wu S., Schäfer M., Dhurkunde R., Capano C. D., 2023, *Astrophys. J.*, 946, 59
- O’Leary R. M., Kocsis B., Loeb A., 2009, *Mon. Not. Roy. Astron. Soc.*, 395, 2127
- O’Shaughnessy R., Gerosa D., Wysocki D., 2017, *Phys. Rev. Lett.*, 119, 011101
- O’Shea E., Kumar P., 2021, *arXiv e-prints*, p. [arXiv:2107.07981](https://arxiv.org/abs/2107.07981)
- Olsen S., Venumadhav T., Mushkin J., Roulet J., Zackay B., Zaldarriaga M., 2022, *Phys. Rev. D*, 106, 043009
- Peters P. C., 1964, *Phys. Rev.*, 136, B1224
- Poisson E., Will C. M., 1995, *Phys. Rev. D*, 52, 848
- Punturo M., et al., 2010, *Class. Quant. Grav.*, 27, 194002
- Rasskazov A., Kocsis B., 2019, *Astrophys. J.*, 881, 20
- Reitze D., et al., 2019, *Bull. Am. Astron. Soc.*, 51, 035
- Rodriguez C. L., Loeb A., 2018, *ApJ*, 866, L5
- Rodriguez C. L., Zevin M., Pankow C., Kalogera V., Rasio F. A., 2016a, *Astrophys. J. Lett.*, 832, L2
- Rodriguez C. L., Zevin M., Pankow C., Kalogera V., Rasio F. A., 2016b, *ApJ*, 832, L2
- Rodriguez C. L., Amaro-Seoane P., Chatterjee S., Kremer K., Rasio F. A., Samsing J., Ye C. S., Zevin M., 2018a, *Phys. Rev. D*, 98, 123005
- Rodriguez C. L., Amaro-Seoane P., Chatterjee S., Rasio F. A., 2018b, *Phys. Rev. Lett.*, 120, 151101
- Romero-Shaw I. M., Lasky P. D., Thrane E., Bustillo J. C., 2020, *Astrophys. J. Lett.*, 903, L5
- Romero-Shaw I. M., Lasky P. D., Thrane E., 2021, *Astrophys. J. Lett.*, 921, L31
- Romero-Shaw I. M., Lasky P. D., Thrane E., 2022, *Astrophys. J.*, 940, 171
- Romero-Shaw I. M., Gerosa D., Loutrel N., 2023, *Mon. Not. Roy. Astron. Soc.*, 519, 5352
- Saini P., Favata M., Arun K. G., 2022, *Phys. Rev. D*, 106, 084031
- Samsing J., 2018, *Phys. Rev. D*, 97, 103014
- Samsing J., D’Orazio D. J., 2018, *MNRAS*, 481, 5445
- Samsing J., Ramirez-Ruiz E., 2017, *ApJ*, 840, L14
- Samsing J., MacLeod M., Ramirez-Ruiz E., 2014, *Astrophys. J.*, 784, 71
- Sathyaprakash B., et al., 2011, in *46th Rencontres de Moriond on Gravitational Waves and Experimental Gravity*. pp 127–136 ([arXiv:1108.1423](https://arxiv.org/abs/1108.1423))
- Silsbee K., Tremaine S., 2017, *Astrophys. J.*, 836, 39
- Stevenson S., Berry C. P. L., Mandel I., 2017, *Mon. Not. Roy. Astron. Soc.*, 471, 2801
- Tagawa H., Kocsis B., Haiman Z., Bartos I., Omukai K., Samsing J., 2021, *Astrophys. J. Lett.*, 907, L20
- Talbot C., Thrane E., 2017a, *Phys. Rev. D*, 96, 023012
- Talbot C., Thrane E., 2017b, *Phys. Rev. D*, 96, 023012
- Venumadhav T., Zackay B., Roulet J., Dai L., Zaldarriaga M., 2020, *Phys. Rev. D*, 101, 083030
- Virtanen P., et al., 2020, *Nature Methods*, 17, 261
- Vitale S., Lynch R., Sturani R., Graff P., 2017, *Class. Quant. Grav.*, 34, 03LT01
- Waskom M. L., 2021, *Journal of Open Source Software*, 6, 3021
- Wen L., 2003, *Astrophys. J.*, 598, 419
- Wes McKinney 2010, in *Stéfan van der Walt Jarrod Millman eds, Proceedings of the 9th Python in Science Conference*. pp 56 – 61, [doi:10.25080/Majora-92bf1922-00a](https://doi.org/10.25080/Majora-92bf1922-00a)
- Wong K. W. K., Franciolini G., De Luca V., Baibhav V., Berti E., Pani P., Riotto A., 2021, *Phys. Rev. D*, 103, 023026
- Zevin M., Pankow C., Rodriguez C. L., Sampson L., Chase E., Kalogera V., Rasio F. A., 2017, *ApJ*, 846, 82
- Zevin M., Samsing J., Rodriguez C., Haster C.-J., Ramirez-Ruiz E., 2019, *Astrophys. J.*, 871, 91
- Zevin M., et al., 2021a, *Astrophys. J.*, 910, 152
- Zevin M., Romero-Shaw I. M., Kremer K., Thrane E., Lasky P. D., 2021b, *Astrophys. J. Lett.*, 921, L43

This paper has been typeset from a  $\text{\TeX}/\text{\LaTeX}$  file prepared by the author.